Theory and validation of the new features in BIEM solver HAMS-MREL

Raghavan, Vaibhav; Metrikine, Andrei V.; Lavidas, George

DOI
10.1007/s40722-025-00431-8

Publication date
2025

Document Version
Final published version

Published in
Journal of Ocean Engineering and Marine Energy

Journal of Ocean Engineering and Marine Energy
https://doi.org/10.1007/s40722-025-00431-8

RESEARCH

Theory and validation of the new features in BIEM solver HAMS-MREL

Vaibhav Raghavan[1] · **Andrei V. Metrikine**[1] · **George Lavidas**[1]

Received: 23 April 2025 / Accepted: 1 September 2025

Abstract
To accelerate the energy transition, offshore renewable energy is increasingly moving toward array deployment. This shift demands accurate, reliable analysis of hydrodynamics and array interactions at low computational cost. Frequency-domain tools, especially those based on the Boundary Integral Equation Method (BIEM), have thus become widely adopted in the renewables community. Hydrodynamic Analysis of Marine Structures-Marine Renewable Energies Lab (HAMS-MREL) is a recently developed open-source multi-body BIEM solver that computes diffraction and radiation problems, yielding hydrodynamic coefficients and excitation forces on structures. The solver has been validated across a range of geometries using experiments, semi-analytical solutions, and cross-model comparisons, demonstrating high accuracy. This study extends HAMS-MREL with several new features—including wave field calculations (free-surface elevation and pressure), global symmetry, irregular frequency suppression, and generalized (dry) modes—all of which have been validated for accuracy and computational efficiency. OpenMP parallelization has been integrated into each feature, delivering significant computational speed-ups ranging from 13.5× to 47.2×.

Keywords HAMS-MREL · Wave fields · Irregular frequency suppression · Global symmetry · Generalized modes · OpenMP parallelization · Mesh convergence

1 Introduction

Frequency-domain numerical methods are widely adopted in offshore renewable energy, particularly for array configuration studies, due to their several advantages: (a) they deliver accurate and reliable predictions at the preliminary design stage, (b) their outputs—namely frequency-dependent hydrodynamic coefficients—are essential for subsequent time-domain simulations, and (c) they require significantly less computational effort compared to high-fidelity models such as Computational Fluid Dynamics (CFD) (Raghavan et al. 2024a, b; Alves 2016). Among these methods, the Boundary Integral Equation Method (BIEM), grounded in linear potential flow theory, stands out as a popular and effective approach. Its reliability is underscored by the extensive use of well-established commercial solvers such as WAMIT (Lee and Newman 2003), WADAM (DNV 2023), OrcaWave (ORCINA 2023), Hydrostar (Veritas 2024), and ANSYS AQWA (ANSYS 2012). These tools have been thoroughly validated through analytical benchmarks, inter-code comparisons, and experimental wave tank testing (Li and Stansby 2023), making them trusted standards in both academic research and industrial practice.

Then there are in-house solvers, such as DIFFRACT (Chau and Taylor 1992), which are neither commercial nor open-source. These solvers have been extensively developed and applied to multi-body BIEM simulations involving Wave Energy Converters (WECs) and WEC farms. For instance, Sun et al. (2016) used DIFFRACT to model the motion and power output of the three-float M4 WEC, treated as a two-body system. Their simulations under regular wave conditions, validated against experimental results, showed accurate predictions for motion and power output at small wave heights. Further studies of small linear arrays comprising 3 to 5 M4 devices also demonstrated up to a 10% increase in power output for certain combinations of wave periods and directions.

✉ Vaibhav Raghavan
v.raghavan@tudelft.nl

Andrei V. Metrikine
A.Metrikine@tudelft.nl

George Lavidas
G.Lavidas@tudelft.nl

[1] Hydraulic Engineering, TU Delft, Stevingweg 1, Delft 2624CN, Zuid Holland, The Netherlands

Published online: 11 September 2025

Wolgamot et al. (2012) applied DIFFRACT to compute frequency-domain responses of three-buoy axisymmetric WEC arrays and showed that layouts optimized for peak absorption at one wave heading often underperform under others. In a follow-up, Wolgamot et al. (2016) incorporated second-order hydrodynamics into a 2×2 square array of truncated cylinders—exploiting near-trapped modes to strengthen inter-device coupling—and demonstrated up to 30% power gains in shallow water.

Li and Stansby (2023) introduced OREGEN-BEM, an OpenMP-parallelized in-house BEM solver validated against OrcaWave, WAMIT, WADAM, and the open-source HAMS (Liu et al. 2018), achieving runtimes comparable to WAMIT and HAMS in single-body cases and at least $1.3\times$ faster performance in multi-body scenarios. In a subsequent application, (Li and Stansby 2024) used OREGEN-BEM to model the M4 WEC with analytical inter-body constraints, reproducing OrcaWave's dynamic responses across a range of wave periods in agreement with experimental data. Later, Li et al. (2024) coupled OREGEN-BEM with the non-potential flow solver OceanWave3D to simulate a moored buoy—finding OREGEN-BEM alone accurate under moderate wave steepness and the hybrid model superior for high-steepness conditions.

Parallel to commercial developments, significant effort has also been devoted to open-source BIEM solvers for multi-body systems. Notable examples include Nemoh 2.x, Nemoh 3.0, and Capytaine, all widely used in the renewable energy research community. These tools compute diffraction and radiation solutions, offering hydrodynamic coefficients, excitation forces, and wave field outputs. Each has distinct strengths and limitations.

Nemoh 2.x (Babarit and Delhommeau 2015), developed at 'Ecole Centrale de Nantes, was the first open-source linear potential flow solver. Released in 2014, it has been applied extensively to array simulations, validated through experiments and cross-model comparisons (Babarit and Delhommeau 2015; Balitsky et al. 2017; Verao Fernandez et al. 2018a, b; Mankle et al. 2019; Chowdhury et al. 2016; Verbrugghe et al. 2017). It uses a source distribution approach and supports a single global symmetry plane, but lacks irregular frequency suppression. Irregular frequencies, arising from ill-conditioned boundary integral equations (Kelly et al. 2022), correspond to sloshing-mode eigenfrequencies derived from the internal Dirichlet problem (Marburg and Amini 2005). These frequencies result from waterplane interactions at the free surface (Liu 2019) and are numerical in nature. Nemoh 2.x also faces high computational demands and limited documentation (Kurnia and Ducrozet 2023). It interpolates the Green's function using large lookup tables (ranging from 64,000 to 200,000 entries) (Sheng et al. 2022), making it computationally intensive. The solver also struggles with thin or overlapping structures, structures with moonpools, and lacks parallel computing support.

Nemoh 3.0 (Kurnia and Ducrozet 2023), released in 2023, addresses several of these issues. It implements an extended BIEM to suppress irregular frequencies, adds more efficient linear solvers (LU, Gauss elimination, GMRES), and improves accuracy with refined Green's function interpolation and integration schemes. These improvements have beenvalidated against Hydrostar. Nemoh 3.0 also models thin elements more reliably, though issues persist with overlapping panels. Despite its enhancements, the solver still lacks parallelization and has limited capabilities for overlapping-body geometries such as Oscillating Water Columns (OWCs).

Capytaine (Ancellin and Dias 2019), a Python-based evolution of Nemoh, offers both source and potential formulations, multiple solvers (LU, GMRES), and OpenMP parallelization. It now supports irregular frequency suppression (Herdayanditya et al. 2024) and a single global symmetry plane. Validation for multi-body problems has been performed, with some studies such as those by Quartier et al. (2024) and Vervaet et al. (2024) showing accurate predictions. Herdayanditya et al. (2024) validated Capytaine against ANSYS AQWA, including suppression of irregular frequencies, pressure and elevation fields. However, challenges remain in modelling overlapping structures like OWCs (Ancellin and Nguyen 2024).

HAMS is computationally much faster than other open-source BIEM solvers such as Nemoh 2.x and Capytaine (Raghavan et al. 2024c; Sheng et al. 2022). HAMS-MREL builds upon the framework of single-body solver HAMS (Liu et al. 2018), to solve multiple-body fluid–structure interaction problems for the diffraction and radiation problem using mixed source/dipole boundary integral equations, to produce the hydrodynamic coefficients and excitation forces. It has been validated with experiments, semi-analytical solutions and cross-model validation for a number of different structural geometries used within the field of renewables. It has OpenMP parallelization implemented, which allows it to be at par or even faster than WAMIT for certain cases.

When considering the available open-source multiple-body BIEM solvers, HAMS-MREL shows significant promise for two aspects: (a) Solving the diffraction and radiation problems for structures with overlapping panels, which is useful for modelling structures with moonpools and wave energy converters such as OWCs. In the work of (Raghavan et al. 2024a), the hydrodynamic coefficients for a floating OWC structure were validated with WAMIT. The piston method was utilized to model the water column in the OWC. The results showed an almost perfect match between the two solvers. Furthermore, in the work of (Raghavan et al. 2024b), a rectangular bottom detached fixed OWC was modelled utilizing a BEM-CFD framework. The piston method

was used to model the water column response while introducing the pressure above the water column as damping, based on the CFD simulations. The model was validated with experiments providing accurate estimates for the RAO and Capture Width Ratio (CWR) within an accuracy of 90–95%. (b) Extensive validation with parallelization - In the work of (Raghavan et al. 2024a), HAMS-MREL was validated with semi-analytical solutions and WAMIT for four cases considering different geometries. This included cylinders and spheres, with one case showing overlapping cylinders (OWC). The results showed that HAMS-MREL matched WAMIT in terms of accuracy for all the considered cases. Additionally, when comparing the parallelization capabilities (considering a direct solver), HAMS-MREL was up to 2–3 times faster than WAMIT for deep water cases.

The present study further expands HAMS-MREL's capabilities by introducing and validating several new features: wave field computations (free-surface elevation and pressure), Response Amplitude Operators (RAOs), a global symmetry plane, suppression of irregular frequencies, and generalized (dry) modes.

By utilizing the RAOs and thus the wave fields, the variation in the free surface elevation/pressure across arrays can be studied. These have applications including studying the interference effects between devices, Shielding effects from arrays, array layout optimization for wave energy converters, Load and motion prediction in coupled analysis, Fatigue analysis etc. The global symmetry feature is useful for reducing the computational effort required, particularly when using large arrays of devices. This will be further enhanced using OpenMP. Suppression of irregular frequencies is beneficial to avoid large over or underestimations in the response of devices. This will be further enhanced at an array level, leading to wrong load estimations or power production estimations. The generalized modes approach allows for modeling structures that are either flexible or constrained. This can be for modeling wave energy converters, such as the flap, which are hinged to the sea bed or attenuators, which have hinges between rigid parts. These can also be utilized for load estimations on slender wave energy converters, referred to as hydroelastic analysis (Guo et al. 2018; van Rij et al. 2017). With all these features, a more accurate estimation of array behavior can be performed, and used for further optimization.

All features have been parallelized using OpenMP to enhance performance. HAMS-MREL v1.0—the current open-source release—already includes parallelized routines for Green's function evaluation, potential solution of linear systems, and sweeping across incident wave directions. These new additions extend parallelization to a broader range of computations, significantly improving overall computational efficiency.

Section 2 outlines the current HAMS-MREL framework, Sect. 3 presents the theoretical development and validation of the new features, and Sect. 4 concludes the study with key findings.

2 Current framework of HAMS-MREL

The framework of HAMS-MREL is written in Fortran 90, with pre and post-processing done in Python. The compilations were performed utilizing Intel OneAPI 2022, with Visual Studio 2019.

HAMS-MREL solves the diffraction and radiation multiple body problem, based on the linear potential flow theory considering relevant boundary conditions. The flow is described through a total complex-valued spatial velocity potential $\phi(\mathbf{x})$ for all considered bodies which can be expressed as the summation of three parts: the complex-valued spatial incident wave potential $\phi_I(\mathbf{x})$, the complex-valued spatial scattered potential $\phi_S(\mathbf{x})$ and the complex-valued spatial radiated potential $\phi_R(\mathbf{x})$. Here, $\mathbf{x}$ refers to the cartesian coordinates (x, y, z). This is shown as (Fig. 1):

$$\phi = \phi_I + \phi_S + \phi_R = \phi_D + \phi_R \tag{1}$$

where ϕ_D is the complex-valued diffraction potential. The potential satisfies the Laplace equation:

$$\nabla^2 \phi = 0 \tag{2}$$

When considering the diffraction and radiation problem, the following boundary conditions are considered (For brevity, the boundary conditions for both the diffraction and radiation problem are given together):

- The free surface boundary condition

$$\frac{\partial \phi_D}{\partial z} = \mu \phi_D, \frac{\partial \phi_j^{(k)}}{\partial z} = \mu \phi_j^{(k)}, z = 0 \tag{3}$$

  where $\mu = \omega^2/g$ is the deepwater wave number with ω being the angular frequency of the incident wave and g is the acceleration due to gravity. Here $\phi_j^{(k)}$ refers to the radiation potential of the fluid velocity field generated by the j^{th} degree of freedom (dof) for the k^{th} body. j = 1,...,6 and k = 1,...,M. $n_j^{(k)}$ is the normal vector in the j^{th} dof for the k^{th} body.
- The body boundary condition

$$\frac{\partial \phi_D}{\partial n} = 0, \frac{\partial \phi_j^{(k)}}{\partial n} = n_j^{(k)}, \text{on } S_B^{(k)} \tag{4}$$

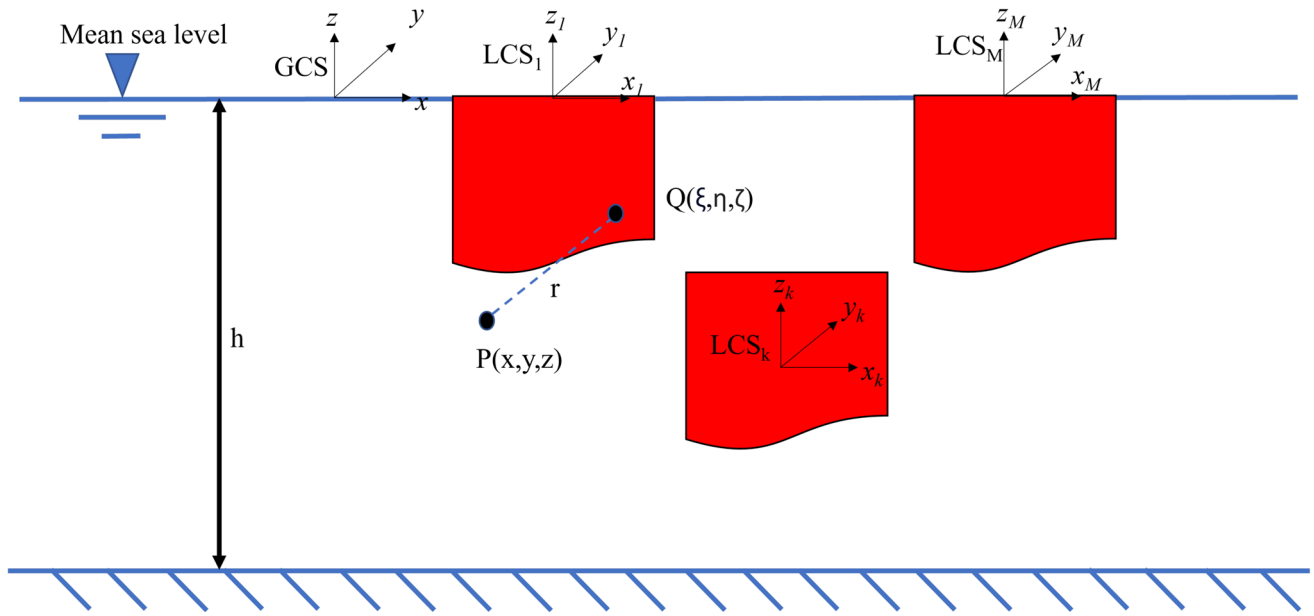

Fig. 1 Definition of the coordinate system for the multiple body interaction problem. GCS refers to the global coordinate system and LCS refers to the local coordinate system per body. Q denotes the source point on the immersed body surface and P denotes the field point anywhere in the fluid domain. (This figure is taken from Raghavan et al. (2024a))

where $S_B^{(k)}$ is the body surface of the k^{th} body. This boundary condition applies to all bodies.

- The sea bottom boundary condition

$$\frac{\partial \phi_D}{\partial z} = 0, \frac{\partial \phi_j^{(k)}}{\partial z} = 0, z = -h, \text{or} \quad z \to \infty \text{ depending on the depth} \tag{5}$$

where h denotes the water depth considering finite depth.

- Sommerfield's radiation condition

$$\lim_{R\to\infty}\left[\sqrt{\mu R}(\frac{\partial \phi_D}{\partial R} - i\mu\phi_D)\right] = 0,$$
$$\lim_{R\to\infty}\left[\sqrt{\mu R}(\frac{\partial \phi_j^{(k)}}{\partial R} - i\mu\phi_j^{(k)})\right] = 0 \tag{6}$$

where R is the horizontal distance from any of the bodies and $'i'$ refers to the imaginary unit with its coefficient referring to the imaginary part of a complex number. Within this formulation, the Sommerfield's radiation condition should be satisfied at large distances from the group of bodies.

The boundary integral equation for the diffraction problem (for the complex-valued scatter potential) considering these boundary conditions with $S_B^T = S_B^{(1)} + S_B^{(2)} + ... + S_B^{(M)}$ is given as follows:

$$2\pi\phi_S(\mathbf{x}) + \iint_{S_B^T} \phi_S(\xi)\left(\frac{\partial G(\xi;\mathbf{x})}{\partial n_\xi}\right) dS_\xi = -\iint_{S_B^T}\left(\frac{\partial \phi_I}{\partial n}\right) G(\xi;\mathbf{x}) dS_\xi \tag{7}$$

Here $\mathbf{x}$ refers to the field point, ξ refers to the source point, G is the Green's function and the subscript $'I'$ indicating the incident wave. Similar to the diffraction problem, the boundary integral equation for the complete radiation problem can be given as follows:

$$2\pi\phi_j^{(k)}(\mathbf{x}) + \iint_{S_B^T} \phi_j^{(k)}(\xi)\left(\frac{\partial G(\xi;\mathbf{x})}{\partial n_\xi}\right) dS_\xi = \iint_{S_B^{(k)}} G(\xi;\mathbf{x}) n_j^{(k)} dS_\xi \tag{8}$$

By utilizing the 'collection' method wherein the centroids of the panels represent the collection points, the boundary integral equation for the diffraction problem (Eq. 7) is discretized into:

$$2\pi\phi_S(\mathbf{x}_i) + \sum_{l=1}^{N_p^T} D_{il}\phi_S(\mathbf{x}_l) = \sum_{l=1}^{N_p^T} S_{il} V_I(\mathbf{x}_l), \quad (i = 1, 2, ..., N_p^T) \tag{9}$$

Here N_p^T is the summation of panels over all bodies. The integrations of the sources and dipoles within the mixed

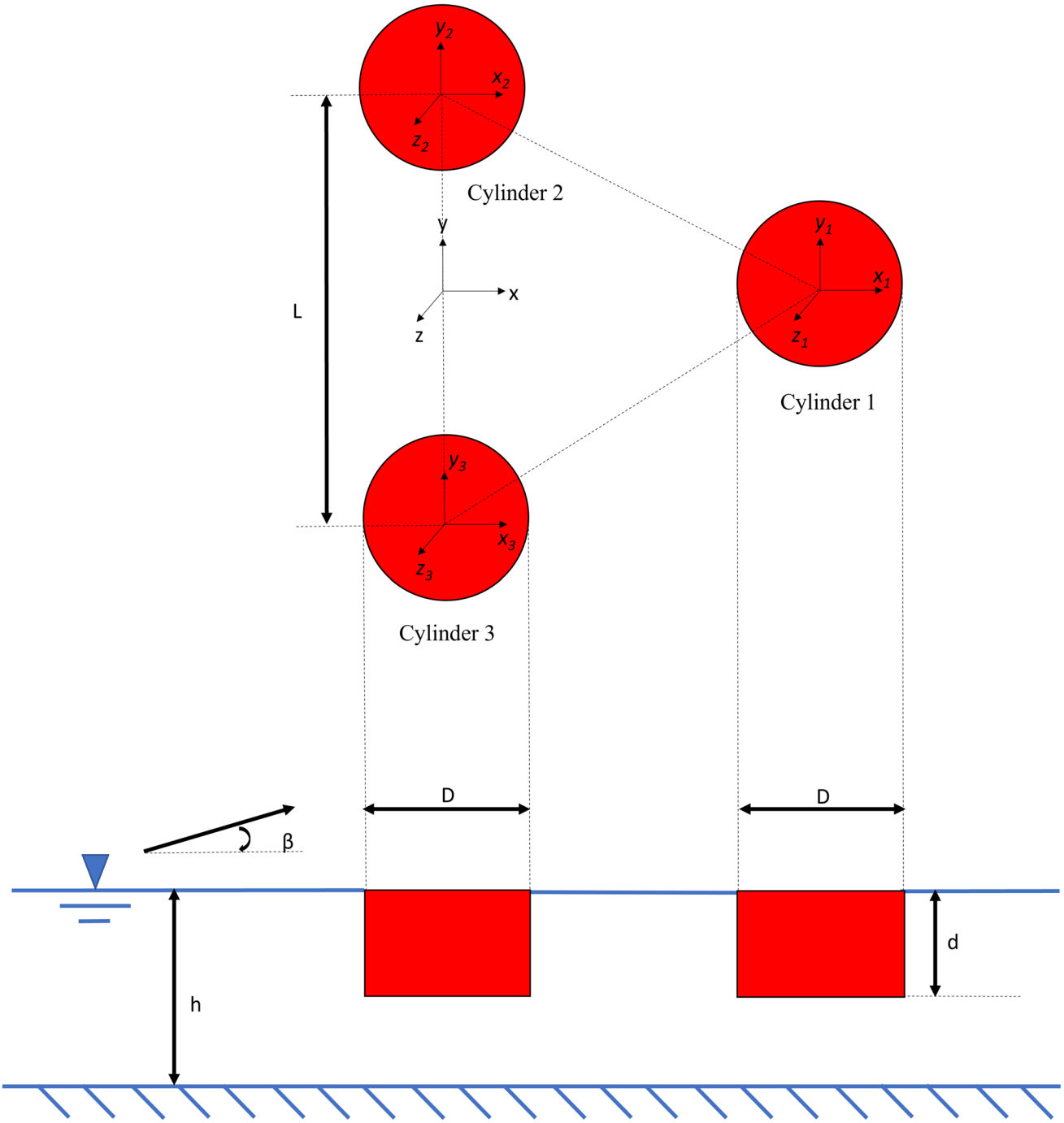

Fig. 2 Three cylinder case – wave fields (This figure is taken from Raghavan et al. (2024a))

source/dipole formulation over each panel for the scattering problem is given as follows:

$$D_{il} = \iint_{S_{B,l}} \frac{\partial G(\xi; \mathbf{x}_i)}{\partial n_\xi} dS_\xi \tag{10}$$

$$S_{il} = \iint_{S_{B,l}} G(\xi; \mathbf{x}_i) dS_\xi \tag{11}$$

and

$$V_I(\mathbf{x}_l) = -\frac{\partial \phi_I}{\partial n}(\mathbf{x}_l) \tag{12}$$

Similarly, the collection method can be applied to the radiation problem and is given as:

$$2\pi\phi_j^{(k)}(\mathbf{x}_i) + \sum_{l=1}^{N_p^T} D_{il}\phi_j^{(k)}(\mathbf{x}_l) = \sum_{m=1}^{N_p^k} S_{im} n_j^{(k)}(\mathbf{x}_m) \tag{13}$$

with $i = 1, 2, ..., N_p^{(M)}$, $j = 1, 2, ..., 6$ and

$$n_j^{(k)}(\mathbf{x}_l) = \frac{\partial \phi_j^{(k)}}{\partial n}(\mathbf{x}_l) \tag{14}$$

This assembly for the radiation problem is done for all M bodies to obtain the final set of linear algebraic equations for all M bodies.

Once the velocity potentials on the body surfaces are obtained, the hydrodynamic coefficients and excitation forces can be computed based on Kashiwagi et al. (2005). By integrating the pressure multiplied by the j^{th} component of the normal vector over the k^{th} body, the hydrodynamic forces acting in the j^{th} dof of the k^{th} body can be computed. These are as follows:

$$E_j^{(k)} = i\omega\rho \iint_{S_B^k} \phi_D n_j^{(k)} dS \tag{15}$$

$$A_{js}^{(k)(q)} + (i/\omega) B_{js}^{(k)(q)} = \rho \iint_{S_B^k} \phi_j^{(q)} n_s^{(k)} dS \tag{16}$$

where $E_j^{(k)}$ is the wave excitation force in the j^{th} dof of the k^{th} body, and $A_{js}^{(k)(q)}$ and $B_{js}^{(k)(q)}$ are the added mass and radiation damping coefficients, respectively, in the s^{th} dof of the k^{th} body due to the j^{th} mode of motion of the q^{th} body.

3 Overview of the new features in HAMS-MREL

For all the new features, the simulations performed in Snellius High Performance Computer (SURF Netherlands) in a 64 GB node with AMD Rome 7H12 processor (3.3 GHz).

3.1 Wave fields

This section focuses on the implementation and validation of wave fields (elevation/pressure) in HAMS-MREL.

3.1.1 Implementation of wave fields

The additional features showcased in the next section are built upon this current framework in HAMS-MREL.

The current version of HAMS-MREL (v1.0) computes the diffraction and radiation potentials for multiple-body interaction problems, as demonstrated in the previous section. This serves as the foundation for extending the theory to wave field computations. Consider a field point $\mathbf{x}$ at which the wave field is to be evaluated. If $\mathbf{x}$ lies on the free surface, HAMS-MREL calculates the corresponding free surface elevation. If $\mathbf{x}$ is located below the free surface, the hydrodynamic pressure at that point is determined.

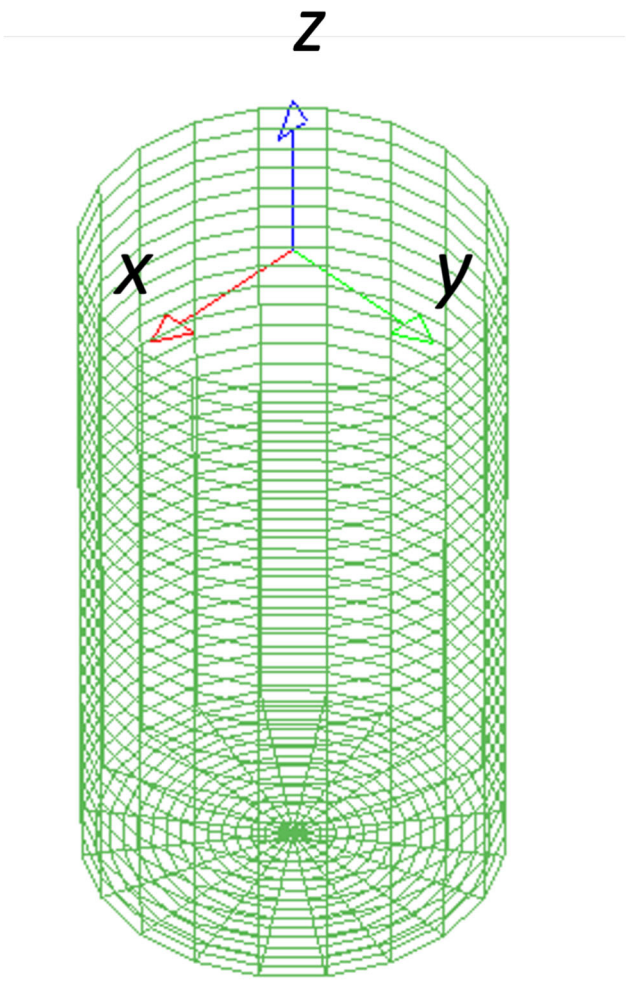

Fig. 3 Cylindrical mesh with 900 panels used in Case 3

The complex-valued hydrodynamic pressure on the body boundary or fluid domain is related to the velocity potential by the linearized Bernoulli equation:

$$p(\mathbf{x}, t) = -\rho \frac{\partial \phi(\mathbf{x}, t)}{\partial t} \tag{17}$$

In the frequency domain, at any field point $\mathbf{x}$, this will be:

$$p(\mathbf{x}) = i\omega\rho\phi(\mathbf{x}) \tag{18}$$

The total velocity potential in HAMS-MREL is defined by:

$$\phi(\mathbf{x}) = \phi_D(\mathbf{x}) - i\omega \sum_{j=1}^{6M} \zeta_j \phi_j(\mathbf{x}) \tag{19}$$

Table 1 Properties of the three cylinder case for obtaining wave fields

Property	Value
Diameter, D (m)	6
Draft, d (m)	10.95
Water depth, h (m)	120
Spacing, L (m)	15
Incident wave angle, $\beta(^\circ)$	0
Number of frequencies, N_ω (–)	100
Amplitude of wave, A (m)	1

where the radiation and diffraction potentials are explained in Sect. 2. ζ_j refers to the amplitude of motion in the j^{th} dof. The body can be evaluated separately for the diffraction and radiation problems and then combined.

Similar to the complex-valued hydrodynamic pressure, the free-surface elevation $\eta(\mathbf{x}, t)$ can also be obtained from the total velocity potential. This is obtained from the dynamic free-surface condition as:

$$\eta(\mathbf{x}, t) = -\frac{1}{g}\left(\frac{\partial \phi(\mathbf{x}, t)}{\partial t}\right)_{z=0} \tag{20}$$

In the frequency domain, this will be:

$$\eta(\mathbf{x}) = \frac{i\omega}{g}\phi(\mathbf{x})_{z=0} \tag{21}$$

3.1.2 Validation and discussion on the implementation

To validate the wave fields in HAMS-MREL, a simulation of a three-cylinder case was run and compared with WAMIT. The free-surface elevation for diffraction and radiation are individually considered here. The case is taken from the work of Raghavan et al. (2024a). The case is shown in Fig. 2 and the mesh is shown in Fig. 3. The properties of the case are shown in Table 1.

The diffraction and radiation fields were independently validated along with the Response Amplitude Operator (RAO). All six degrees of freedom per cylinder were considered in the calculation. For brevity, only the RAO $\zeta_1^{(1)}$ and phase $\psi_1^{(1)}$ is shown in Fig. 4. It is observed that HAMS-MREL matches well with WAMIT. A small spike is observed close to 2.5 s, which is essentially an irregular frequency. Similar results were obtained for other degrees of freedom.

The non-dimensional diffraction and radiation-free-surface elevation validation is shown in Figs. 5 and 6, respectively. The diffraction and radiation fields have been made non-dimensional based on WAMIT manual (Lee and Newman 2006) as shown in Eq. 22

$$\frac{\eta_{diff}}{A} = \frac{-\phi_D}{igA/\omega} \tag{22}$$

$$\frac{\eta_j^{(k)}}{A} = \frac{\mu\phi_j^{(k)}}{L^n} \tag{23}$$

where η_{diff} and $\eta_j^{(k)}$ are the free-surface elevation for the diffraction and j^{th} mode, k^{th} body radiation respectively. L is the length scale, taken as 1.0 in this case. $n = 0$ for $j = 1,2,3$ and $n = 1$ for $j = 4,5,6$.

In all cases, the Mean Squared Error (MSE) was less than 2 % across the considered domain. For the considered case, 10,000 field points (N_f) were considered as field points for the computation of the free surface elevation field for each of the 100 frequencies (N_ω).

The computational gain of 23 times is observed from Table 2. It should be noted that for the case 'No parallelization', there is no parallelization applied for the computation of Green's function, solving the linear set of equations for the potential and the computation of the wave fields.

3.2 Global symmetry

This section focuses on the implementation and validation of global symmetry applied in HAMS-MREL.

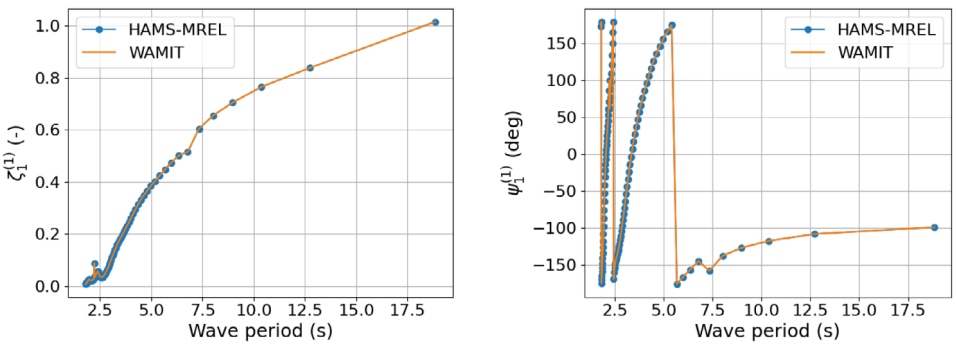

Fig. 4 RAO and phase for surge – Cylinder 1

(a) RAO $\zeta_1^{(1)}$ (b) Phase $\psi_1^{(1)}$

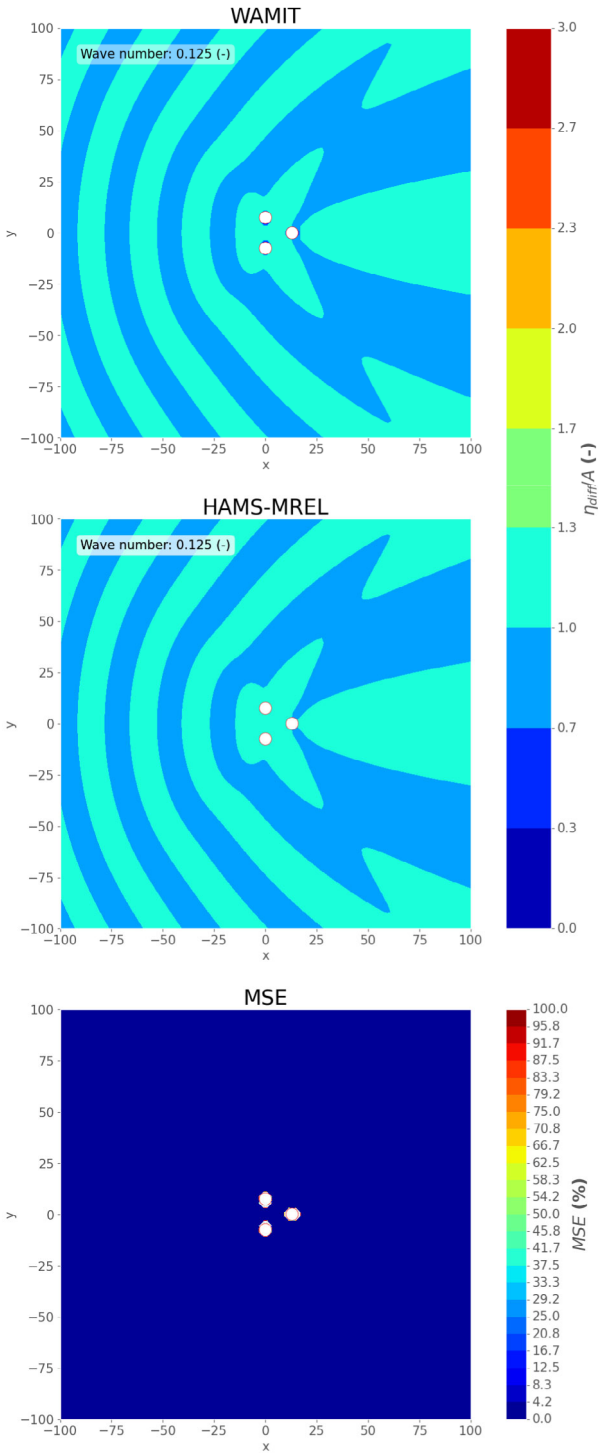

(a) Non-dimensional Diffraction free surface elevation η_{diff}/A for wavenumber ν=0.125

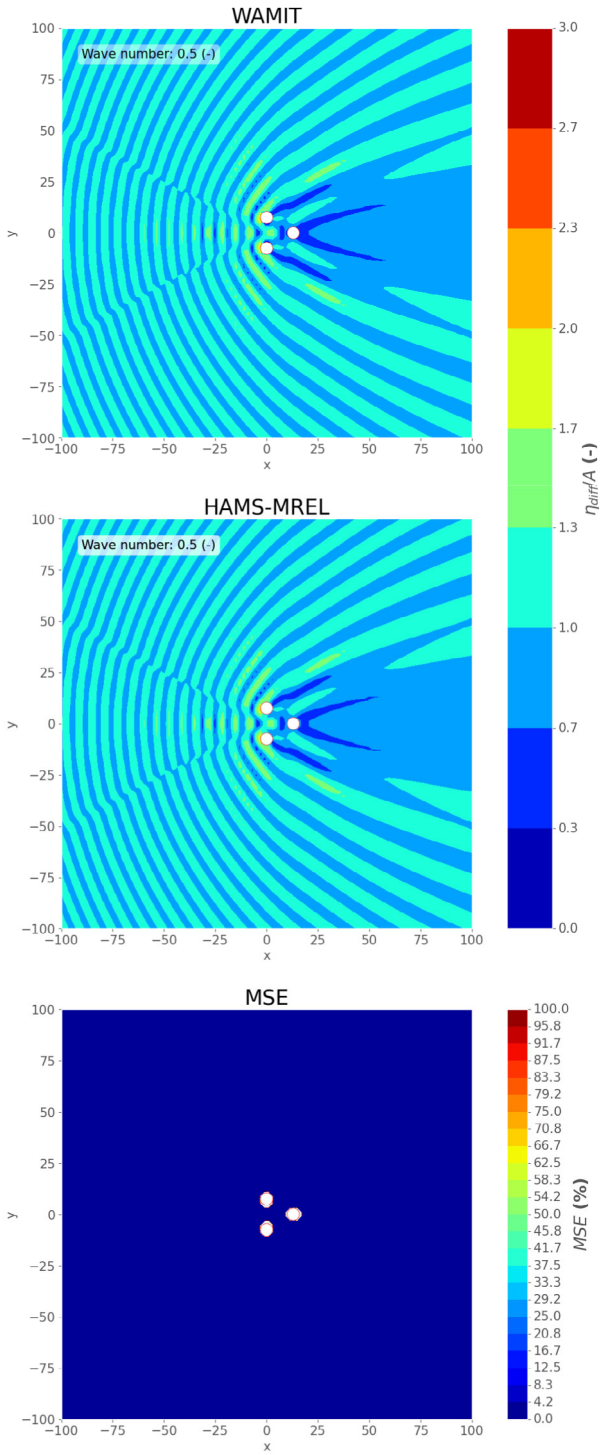

(b) Non-dimensional Diffraction free surface elevation η_{diff}/A for wavenumber ν=0.5

Fig. 5 Validation of the non-dimensional diffraction free surface elevation, the first row shows the WAMIT results, second row the HAMS-MREL, and the third row the Mean Square Errors (MSE) between the models

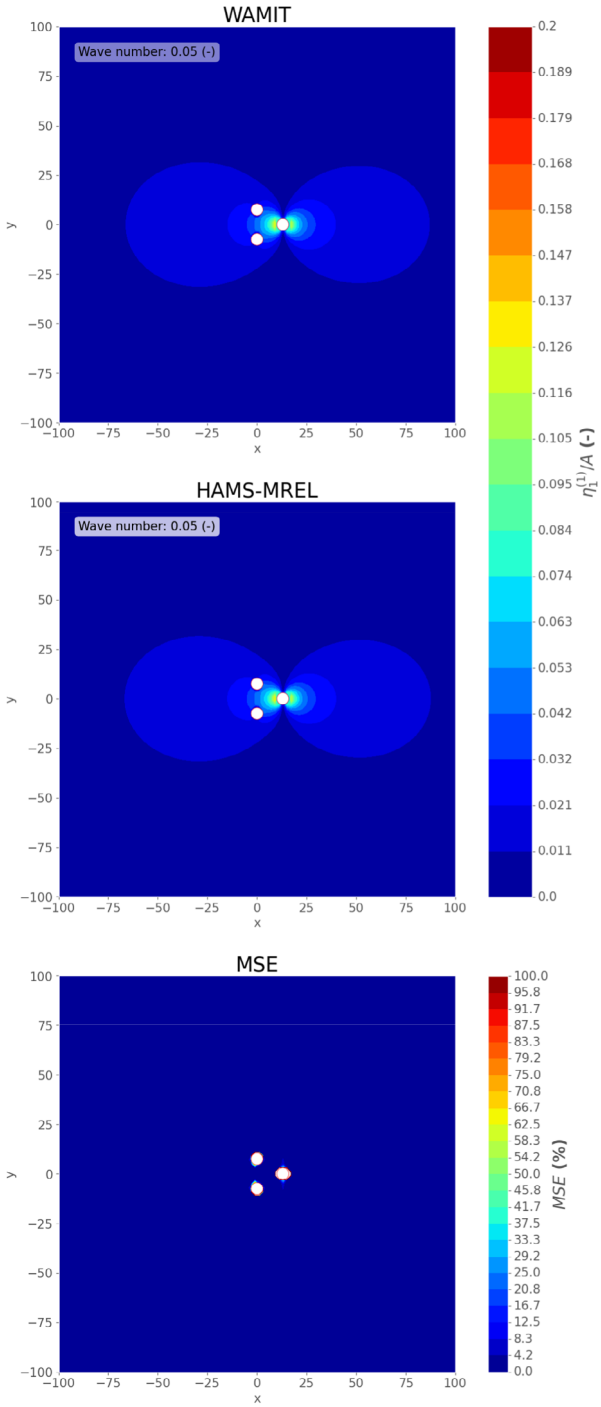

(a) Non-dimensional Radiation free surface elevation $\eta_1^{(1)}/A$ for wavenumber ν=0.05

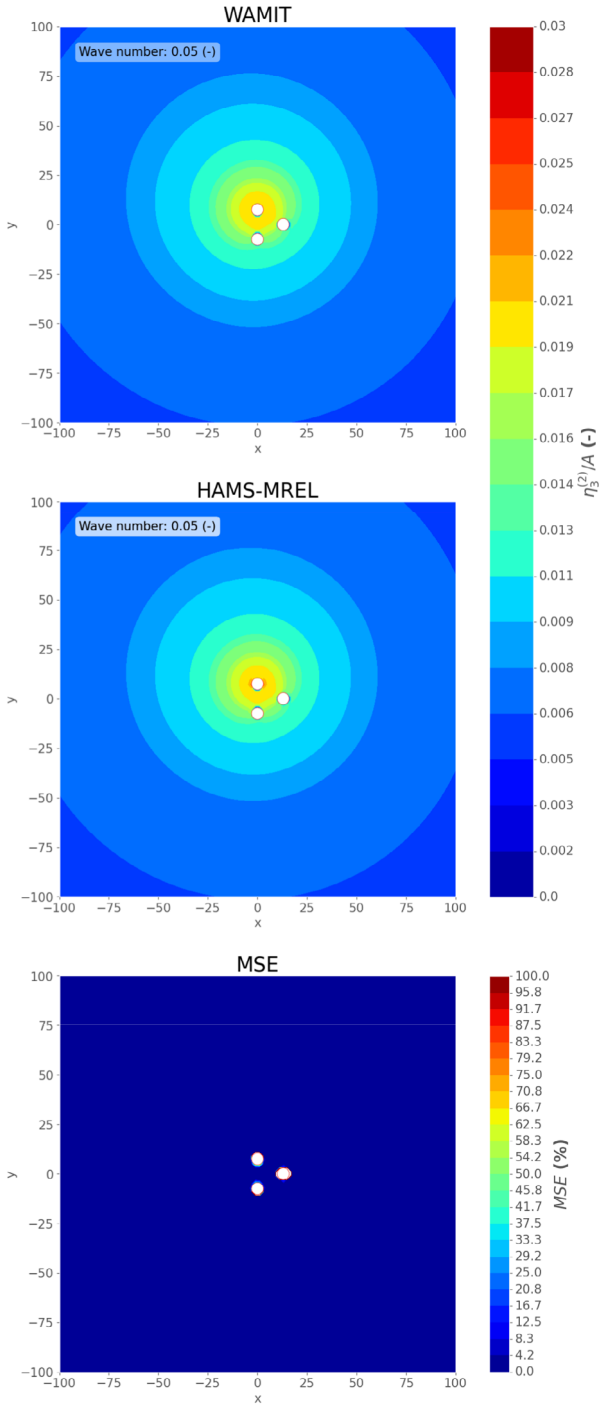

(b) Non-dimensional radiation free surface elevation $\eta_3^{(2)}/A$ for wavenumber ν=0.5

Fig. 6 Validation of the non-dimensional Radiation free surface elevation, the first row shows the WAMIT results, second row the HAMS-MREL, and the third row the Mean Square Errors (MSE) between the models

Table 2 Computation time for the simulations (Wave fields)

Simulation	N_ω	N_f	Time/frequency (sec)	Computation gain (–)
No parallelization (1 core)	100	10,000	2700	1.0
Parallelization (32 cores)	100	10,000	124	23.0

3.2.1 Implementation of global symmetry

The computational efficiency of the solution from HAMS-MREL can be significantly improved by utilizing symmetry. With the current implementation, a single global plane of symmetry (either along x or y) can be utilized (Liu et al. (2018); Matsui et al. (1987). The discretized form of the boundary integral equation (see Eq. 9 and Eq. 13) can be expressed as:

$$[A]\{\phi\} = \{B\} \tag{24}$$

Considering a single plane of symmetry, it is possible to partition the matrix A, vector ϕ and matrix B (see Fig. 7, where the partition is made about $y=0$. This indicates that for the panels in $+y$, the vector with the potential is given as ϕ_2. For the panels in $-y$, the vector with the potential is given as ϕ_1). This can be expressed as:

$$[A] = \begin{bmatrix} A_{11} & A_{12} \\ A_{21} & A_{22} \end{bmatrix} \tag{25}$$

$$\{\phi\} = \{\,\phi_1\ \phi_2\,\}^T \tag{26}$$

$$\{B\} = \{\,B_1\ B_2\,\}^T \tag{27}$$

where A_{11} is the submatrix of the coefficients associated with the discretization of boundary region 1, while A_{12} is the corresponding submatrix from the coupling between the boundaries 1 and 2. ϕ_1 and ϕ_2 are the components of the velocity potential corresponding to elements in boundaries 1 and 2 respectively. Similarly, B_1 and B_2 are the right-hand side vectors associated with boundaries 1 and 2, respectively. Furthermore, the following relations can be employed in the calculation:

$$A_{11} = A_{22},\ A_{12} = A_{21} \tag{28}$$

To reduce the number of linear equations to be solved, an orthogonal transformation matrix $[R]$ can be utilized such that:

$$[\widehat{A}] = \frac{1}{\gamma}[R][A][R] \tag{29}$$

$$\{\widehat{\phi}\} = [R]\{\phi\} \tag{30}$$

$$\{\widehat{B}\} = [R]\{B\} \tag{31}$$

with $\gamma = 2$, since there are two regions due to a single plane of symmetry. The transformation matrix is taken from Chau (1989).

Table 3 Properties of the Three cylinder case for symmetry

Property	Value
Diameter, D (m)	6
Draft, d (m)	1.5
Water depth, h (m)	120
Spacing, L (m)	18
Incident wave angle, $\beta(^\circ)$	0
Number of frequencies, N_ω (–)	300

$$R = \begin{bmatrix} 1 & 1 \\ 1 & -1 \end{bmatrix} \tag{32}$$

The transformation enables the linear system into a simplified diagonal form:

$$\begin{bmatrix} \widehat{A}^{(1)} & 0 \\ 0 & \widehat{A}^{(2)} \end{bmatrix} \begin{bmatrix} \widehat{\phi}^{(1)} \\ \widehat{\phi}^{(2)} \end{bmatrix} = \begin{bmatrix} \widehat{B}^{(1)} \\ \widehat{B}^{(2)} \end{bmatrix} \tag{33}$$

From this $\{\widehat{\phi}\}$ can be obtained. Then using Eq 31, the potential $\{\phi\}$ can be obtained.

3.2.2 Validation and discussion on the implementation

The simplest example to demonstrate this is a single row of point absorber devices. This is shown in Fig. 8, where three cylinders are considered. The mesh for one of the cylinders is shown in Fig. 9a

Symmetry about $y=0$ is considered here as shown in Fig. 8. Four simulations are performed in HAMS-MREL to demonstrate the computational gain both from the use of symmetry with and without parallelization. The four simulations are:

- No sym no par - No symmetry and no parallelization - **Base case**
- No sym par - No symmetry with parallelization
- Sym no par - Symmetry with no parallelization
- Sym par - Symmetry with parallelization

For brevity, only the results of the hydrodynamic coefficients and excitation forces for heave for Cylinder 1 are shown in Fig 10. As observed, all four simulations give the same result, thus validating the implementation of global symmetry in HAMS-MREL. A spike is observed close to

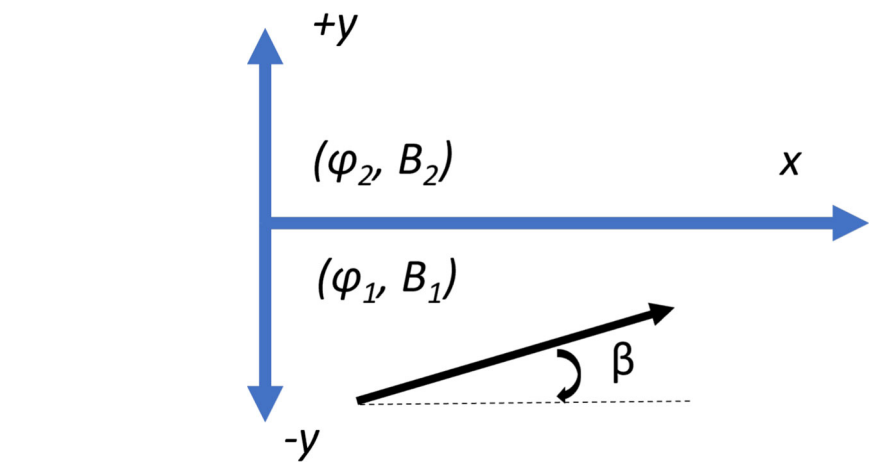

Fig. 7 Symmetry partitioning - symmetry plane $y=0$

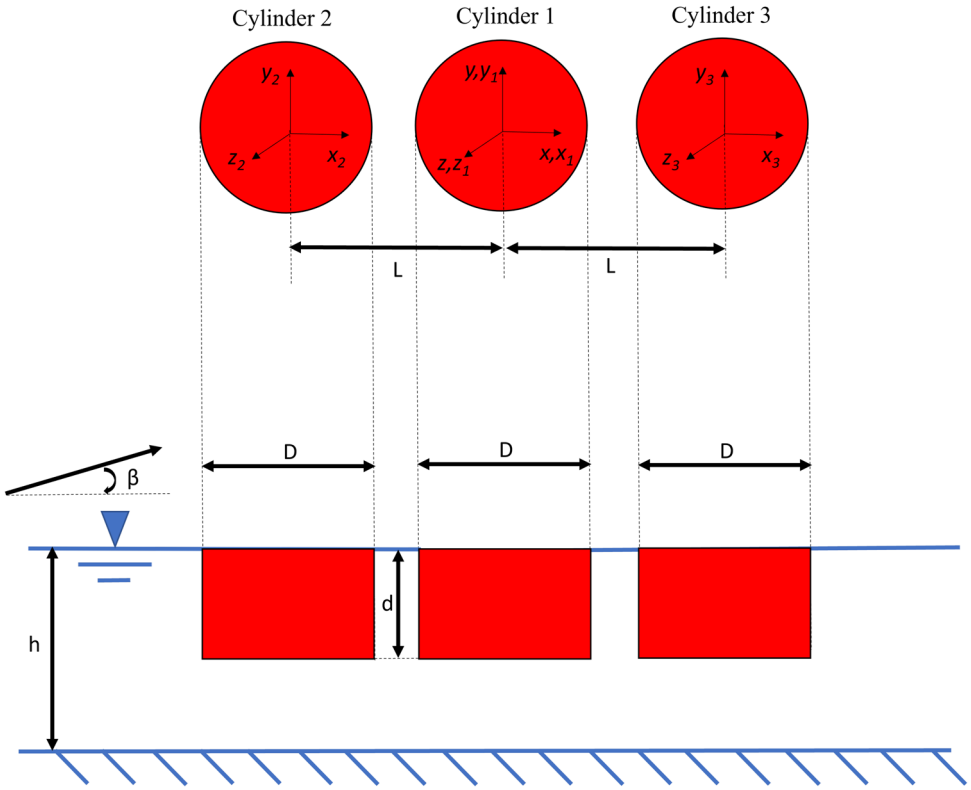

Fig. 8 Three cylinder case

the wave period of 2 s, due to the presence of an irregular frequency. The suppression of this is demonstrated in the next section. The computational time is summarized in Table 4. Parallelization utilized 32 cores.

Significant computational gains are observed, wherein using both symmetry (one plane) and parallelization, the simulation can be speeded up by a factor of 47.2.

3.3 Suppression of irregular frequency

This section focuses on the implementation and validation of the suppression of irregular frequencies in HAMS-MREL. The three-cylinder case, as used in the previous section, is also utilized for the validation study here.

3.3.1 Implementation in HAMS-MREL

When solving mixed source-dipole BIE in HAMS-MREL, substantial errors can occur at 'irregular frequencies'. This is observed as a significant jump or dip in the hydrodynamic coefficients and excitation forces, and can result in unrealistic estimations of the response of floating structures.

The single body BIE solver HAMS is capable of tackling this by discretizing the free surface within the body and solving an extended boundary integral equation problem (Liu

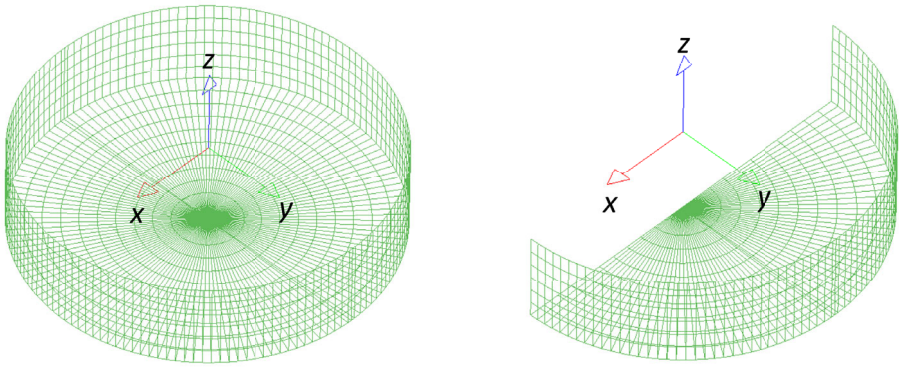

Fig. 9 Cylinder mesh and half cylinder mesh - Symmetry

(a) Whole cylinder mesh

(b) Half cylinder mesh

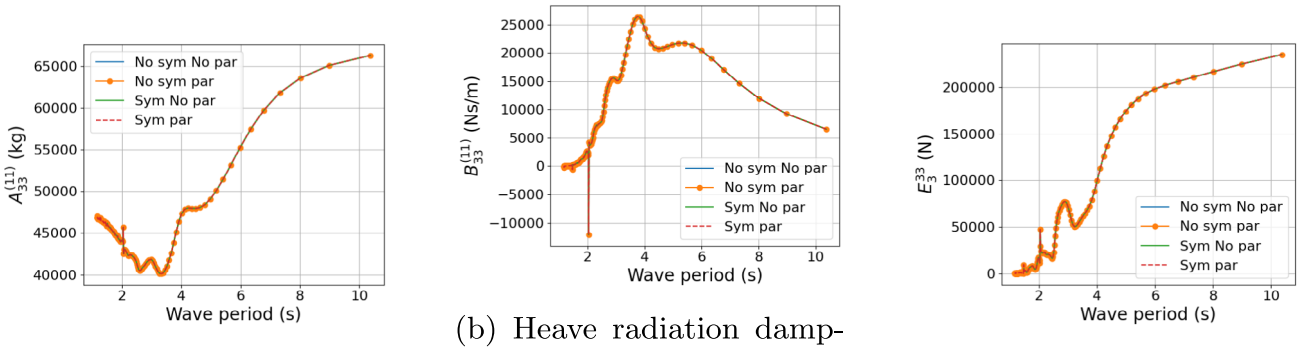

(a) Heave added mass

(b) Heave radiation damping

(c) Heave excitation force

Fig. 10 Hydrodynamic coefficients and excitation forces for heave for Cylinder 1 - Symmetry

Table 4 Computation time for the simulations (Symmetry)

Simulation	N_P^T	N_ω	Time/frequency (sec)	Computation gain (–)
No sym no par	7344	300	2405	1.0
No sym par	7344	300	185	13.0
Sym no par	3672	300	852	2.9
Sym par	3672	300	51	47.2

2019). In this part, solutions are discussed for the suppression of irregular frequencies considering the multiple-body interaction problem, which has been developed here.

An extended BIE which adapts the method from HAMS and incorporates the body boundary condition wherein when one body is in motion in a certain degree of freedom, the other bodies are stationary., is developed and utilized. It assumes that the potentials in the interior of the water plane are zero. This is only performed for bodies where the input waterplane mesh is provided (In HAMS-MREL, it is possible to provide the water plane mesh for specific bodies). By applying Green's equation in the interior of the floating body, additional BIE are introduced which are combined with the conventional BIEs. The extended equation to obtain the scattered potential for body k, k = 1,...,M, should consider the contribution from all the available waterplane meshes (S_{WP}). The boundary integral equation considering this with $S_B^T = S_B^{(1)} + S_B^{(2)} + ... + S_B^{(M)}$ can then be given as follows:

$$\iint_{S_B^T} \phi_S(\mathbf{x}) \left(\frac{\partial G(\xi;\mathbf{x})}{\partial n_\xi} \right) dS_\xi = -\iint_{S_B^T} \left(\frac{\partial \phi_I(\xi)}{\partial n} \right) G(\xi;\mathbf{x}) dS_\xi \tag{34}$$

Here $\mathbf{x}$ refers to the field point and belongs to the water plane meshes ($S_{WP}^T = S_{WP}^{(1)} + S_{WP}^{(2)} + ... + S_{WP}^{(M)}$), ξ refers to the source point and belongs to S_B^T.

Similar to the diffraction problem, the boundary integral equation for the complete radiation problem can be given as follows:

$$\iint_{S_B^T} \phi_j^{(k)}(\mathbf{x}) \left(\frac{\partial G(\xi;\mathbf{x})}{\partial n_\xi} \right) dS_\xi = \iint_{S_B^T} G(\xi;\mathbf{x}) n_j^{(k)} dS_\xi \tag{35}$$

Considering the boundary condition on the body surface (see Eq. 4), this can be reduced to the following equation:

$$\iint_{S_B^T} \phi_j^{(k)}(\mathbf{x}) \left(\frac{\partial G(\xi;\mathbf{x})}{\partial n_\xi} \right) dS_\xi = \iint_{S_B^{(k)}} G(\xi;\mathbf{x}) n_j^{(k)} dS_\xi \tag{36}$$

Here $\phi_j^{(k)}$ refers to the radiation potential of the fluid velocity field generated by the j^{th} degree of freedom (dof) for the k^{th} body. j = 1,...,6 and k = 1,...,M. $n_j^{(k)}$ is the normal vector in the j^{th} dof for the k^{th} body. When the k^{th} body is in motion, all the other bodies are assumed to be stationary.

Considering the total number of elements as N_{WP}^T for all the water plane meshes and N_P^T for all the considered bodies, a set of overdetermined linear algebraic equations can be obtained as follows:

$$[A]_{(N_{WP}^T + N_P^T) X N_P^T} \{\phi\}_{N_P^T} = [B]_{(N_{WP}^T + N_P^T) X N_P^T} \tag{37}$$

The least squares method implemented for solving the set of linear algebraic equations is implemented here. OpenMP parallelization has been applied in HAMS-MREL when solving the extended BIEM problem. This is an extension of the existing OpenMP implementation, wherein the parallelization capabilities are utilized for the calculation of the Green's functions as well as solving the final overdetermined set of algebraic equations per incident wave frequency. The implementation has also been done in such a way that it is possible to choose, for which bodies the waterplane mesh can be used. This provides flexibility, when analysing bodies of different geometries/sizes, where the occurrence of the irregular frequency can be at different frequencies.

3.3.2 Validation and discussion on the implementation

To validate the suppression of irregular frequencies with HAMS-MREL, the three cylinder case from the previous section (see Fig. 8) is utilized. It was observed from Fig. 10, that a spike was observed close to 2 s. The waterplane mesh is shown in Fig. 11. To make a comparison with and without the suppression of irregular frequencies, three different simulations were preformed in HAMS-MREL:

- Simulation 1 - No suppression of irregular frequencies (No-IR)

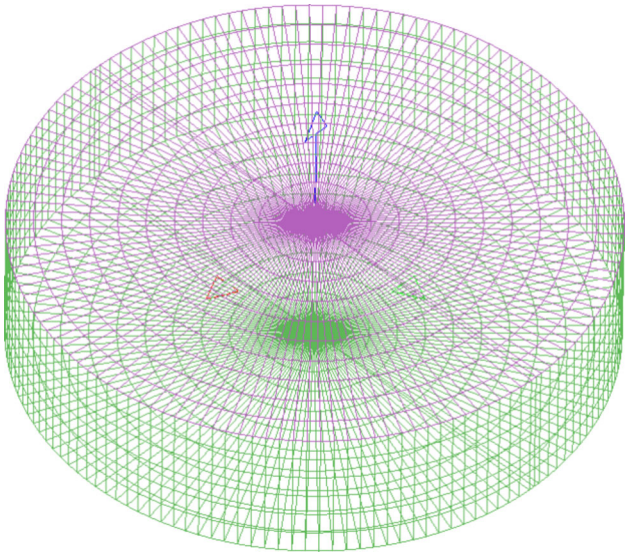

Fig. 11 Water plane mesh (pink) together with the cylinder mesh (green)

- Simulation 2 - Suppression of irregular frequencies for Cylinder 1 and 2 (IR-2)
- Simulation 3 - Suppression of irregular frequencies for all cylinders (IR-all)

The results are shown in Fig. 12. When considering the three cylinder case with no irregular frequency suppression, it is observed that the irregular frequency occurs at around 2 s for all the cylinders. This can be seen in the 'No-IR' simulation in Fig. 12(a)-(i). When considering Simulation 2, wherein the waterplanes are only utilized for Cylinder 1 and 2, it is observed that the irregular frequency is suppressed (see Fig. 12(a)-(f)) while it is not suppressed for Cylinder 3 (see Fig. 12(g)-(i)). Furthermore, it can be observed that when the waterplane mesh is used in all cylinders, the irregular frequency for each cylinder is suppressed. The computational time utilized by HAMS-MREL for the simulations is shown in Table 5. 300 frequencies were considered for each simulation. N^T is the total number of panels in each simulation.

Furthermore, the parallelization capabilities were compared for the case where the water plane mesh was utilized for all three cylinders, to show the computational gain from the parallelization. It is observed that with utilizing 32 cores, a computational gain of 13.5 times can be achieved with the implementation. This is very similar to what was observed with HAMS-MREL (see Raghavan et al. (2024a)), where a computational gain of 14 was observed for the considered finite depth cases.

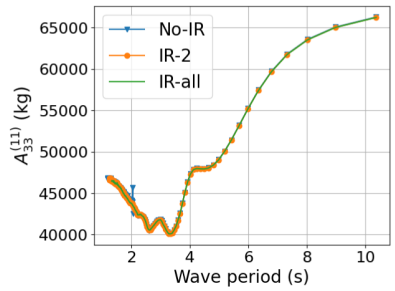

(a) Cyl 1 - Heave added mass

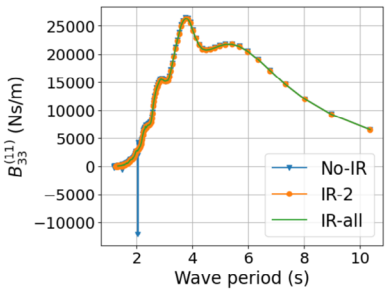

(b) Cyl 1 - Heave radiation damping

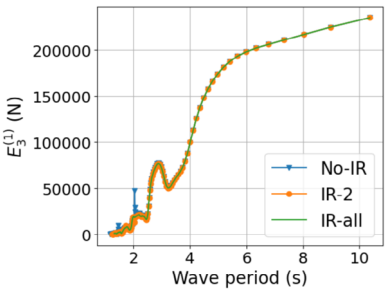

(c) Cyl 1 - Heave excitation force

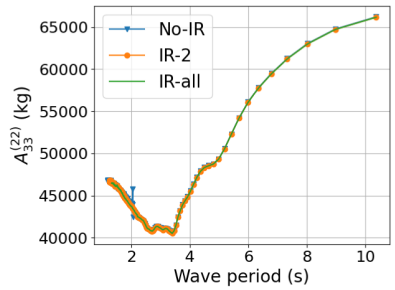

(d) Cyl 2 - Heave added mass

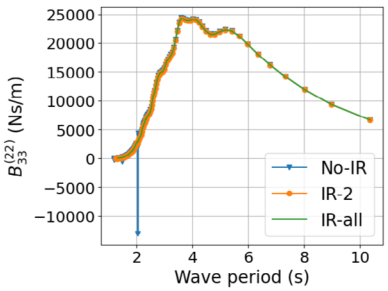

(e) Cyl 2 - Heave radiation damping

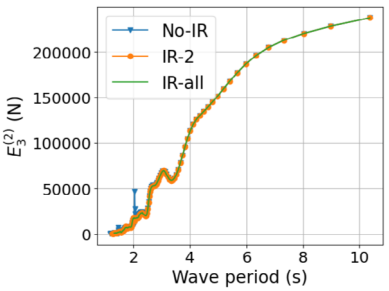

(f) Cyl 2 - Heave excitation force

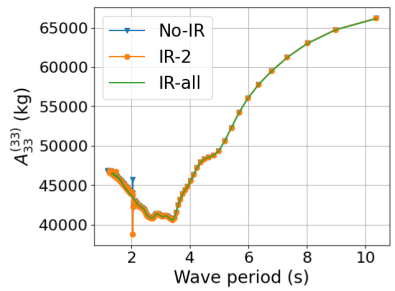

(g) Cyl 3 - Heave added mass

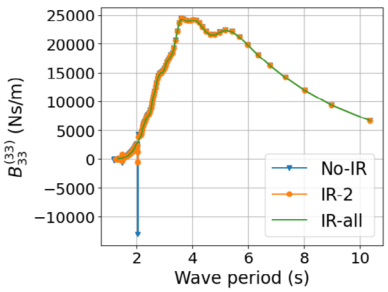

(h) Cyl 3 - Heave radiation damping

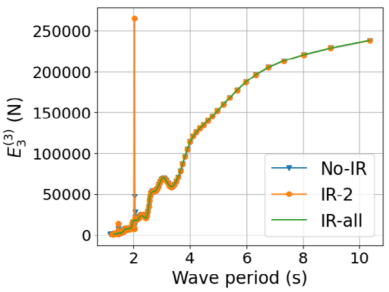

(i) Cyl 3 - Heave excitation force

Fig. 12 Hydrodynamic coefficients and excitation forces for heave for the three cylinder case

Table 5 Computation time for the simulations (suppression of irregular frequencies)

Simulation	N_P^T	N_{WP}^T	N^T	N_ω	Parallelization	Time/frequency (sec)
Simulation 1	7344	0	7344	300	Yes	185
Simulation 2	7344	3168	10,512	300	Yes	209
Simulation 3	7344	4572	11,916	300	Yes	233
Simulation 3	7344	4572	11,916	300	No	3150

3.4 Generalized modes (dry modes) approach

This section focuses on the generalized modes approach, which can be used to model flexible structures or structures with constraints, an example of such bodies are attenuator/terminators wave energy converters, and/or large floating bodies with several hinged components. In order to incorporate any generic motion of the structure, the body boundary condition in the BIEM problem needs to be modified. This is demonstrated as follows. This is based on the dry modes approach introduced in Newman (1994).

3.4.1 Body boundary condition for the first order boundary value problem

The body boundary condition (Eqn 4) can be expressed as a general expression:

$$\frac{\partial \phi_j^{(k)}}{\partial n} = \mathbf{S_j^{(k)}}.\mathbf{n^{(k)}} \tag{38}$$

where $\mathbf{S_j^{(k)}}$ is a 3D vector shape function of the k^{th} body, with cartesian components $u_j^{(k)}$, $v_j^{(k)}$, $w_j^{(k)}$ and $\mathbf{n^{(k)}} = (n_x^{(k)}, n_y^{(k)}, n_z^{(k)})$ is the normal vector projecting from the k^{th} body towards the fluid (Newman 1994). In general, for the rigid body translational degrees of freedom ($j = 1, 2, 3$), the shape function is unit vector in the corresponding direction, and for the rigid body rotations (j=4, 5, 6), $\mathbf{S_j} = \mathbf{S_{j-3}} \times \mathbf{r}$, where $\mathbf{r}$ is the lever arm vector with respect to a rotation center (Newman 1994; Sismani and Loukogeorgaki 2020).

The projection of the normal vector can then be written as:

$$\mathbf{S_j^{(k)}}.\mathbf{n^{(k)}} = u_j^{(k)} n_x^{(k)} + v_j^{(k)} n_j^{(k)} + w_j^{(k)} n_z^{(k)} \tag{39}$$

Therefore, by deriving this vector shape function for any additional mode/degree of freedom, the radiation and diffraction problem can also be solved considering this degree of freedom in HAMS-MREL. The vector shape function can represent general mode shapes corresponding to structural deflections, the motions of the interior free surfaces inside moonpools, or multiple bodies with constraints (Lee and Newman 2003).

To demonstrate this approach in HAMS-MREL, the rigid flap from the work of Van'T Hoff Van (2009) is taken, which has been validated with scaled experiments. The derivation of the shape function has been done in Raghavan et al. (2024d). Therefore, the shape function is summarized here the results for the hydrodynamic coefficients and excitation forces are shown.

Table 6 Properties of the flap(all dimensions in m)

Part	Dimension ($W \times T \times H$)
Flap top	
Rectangular box	$18 \times 1.8 \times 8.5$
Triangular box	$18 \times 0 - 1.8 \times 0.9$
Flap bottom	
Rectangular box	$18 \times 1.8 \times 1.5$

3.4.2 Case study description-flap

The flap is modelled as a two-body problem, where the top and bottom are two different bodies. The geometry of the flap is shown in Fig 14. The flap top combines two geometries, a rectangular box and a triangular box, while the flap bottom, which is rigidly fixed to the sea bottom, is composed of a rectangular box. The dimensions of these parts are shown in Table 6. The hinge is located at $L_s = 8.9$ m from the free surface. The water depth is 10.9 m, thus the hinge being at 2 m above the sea bottom.

xyz is the global coordinate system. $x_l y_l z_l$ is the local coordinate system located at the top of the flap and coincides with the global coordinate system, $x_d y_d z_d$ is the deformed coordinate system due to the flap's unit rotation θ. The flap is aligned such that the width (W) is along the Y axis. The surface of the flap is discretized into panels.

The shape function for the additional degree of freedom/mode shape for the flap top is given as:

$$\mathbf{S_7^{(1)}} = (L_s + z, 0, -x) \tag{40}$$

Since the flap bottom is stationary, the shape function for the bottom is a null vector.

$$\mathbf{S_7^{(2)}} = (0, 0, 0) \tag{41}$$

These are based on Raghavan et al. (2024d). Using this as the body boundary condition for the additional pitch motion about the hinge, the radiation and diffraction problems can be solved to obtain the hydrodynamic coefficients and excitation forces.

3.4.3 Validation and discussion

A cross-model validation with the commercial solver WAMIT was conducted. As previously mentioned, the geometry and results for the hydrodynamic coefficients and excitation force for the flap were adopted from the study by Van'T Hoff Van (2009), as they have been experimentally validated. It is important to note that Van'T Hoff used a slightly lower mesh resolution compared to the converged mesh resolution recommended by WAMIT, due to the minimal impact

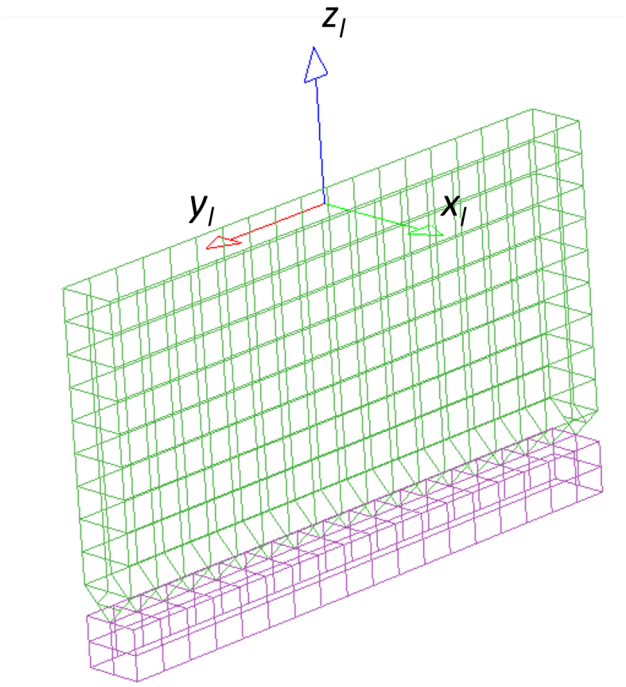

Fig. 13 Mesh of the flap in HAMS-MREL with 518 panels - top (green) and bottom (pink) - from Raghavan et al. (2024d)

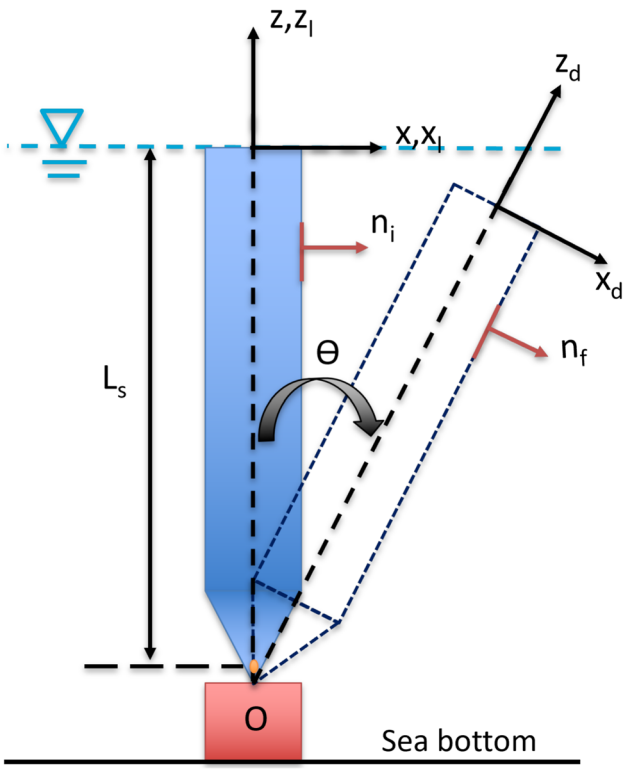

Fig. 14 Schematic representation of rotation of the flap (from Raghavan et al. (2024d))

of mesh resolution on the final results. For this initial comparison, the same mesh resolution (518 panels for both flap top and bottom) utilized by WAMIT was also implemented in HAMS-MREL (Fig. 13).

In the WAMIT model, the flap was represented as a two-body problem. The flap top (see Fig. 14) was assigned a single degree of freedom in pitch with its rotation center located at the hinge ($z = -8.9$ m), while the flap bottom was treated as stationary, thus only diffraction effects were considered. Lower-order panels were utilized for all simulations to solve both diffraction and radiation problems.

The resulting hydrodynamic coefficients, specifically the added mass coefficient and radiation damping coefficient, are illustrated in Figs. 15 and 16, respectively. Comparing the added mass coefficient ($A_{77}^{(11)}$) computed by both solvers, results are very close within the range of 1 to 6 s. Below 1 s, HAMS-MREL slightly overestimates the coefficient. Between 6 s and 14 s, HAMS-MREL shows a minor overestimation of approximately 5.

For the radiation damping coefficient ($B_{77}^{(11)}$), the results from both solvers are generally in good agreement, although HAMS-MREL slightly overestimates the coefficient near the peak at around 5 s.

Excitation force results ($E_7^{(1)}$) are presented in Fig. 17. Both solvers yield closely matched results, with HAMS-MREL slightly overestimating by approximately 5% near the peak occurring at around 6 s.

An unusual peak is observed at the short period of 1 s in both the radiation damping coefficient and excitation force, although it is less prominent in the added mass coefficient. This anomaly can be attributed to an irregular frequency effect, typically observed at high wave frequencies. Such effects can be mitigated by employing a waterplane mesh alongside the hull mesh and solving the extended boundary value problem, as discussed in Sect. 3.3. However, addressing this is beyond the scope of the current section.

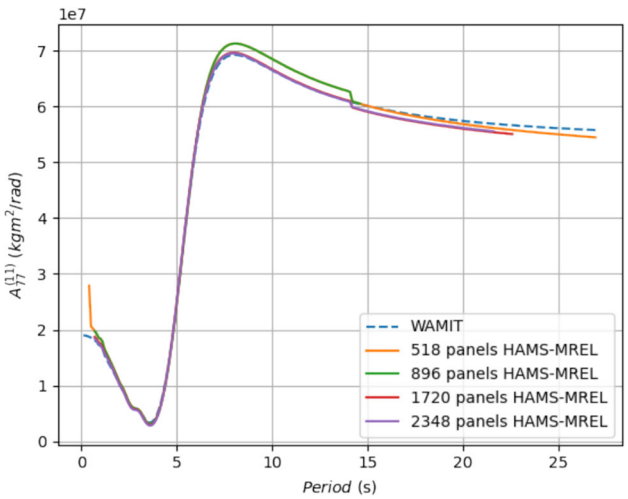

Fig. 15 Added mass flap $A_{77}^{(11)}$

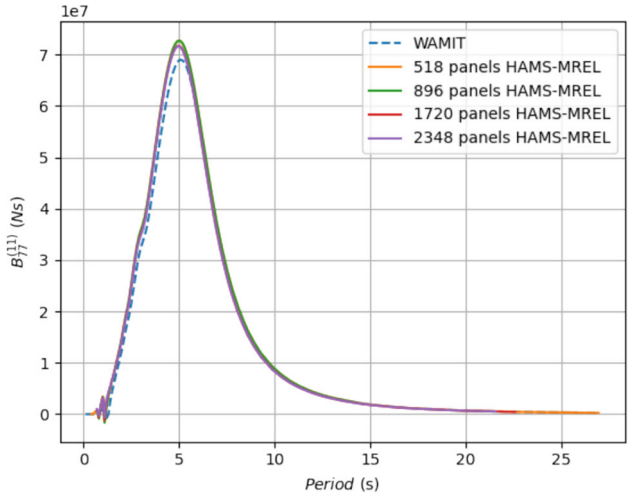

Fig. 16 Radiation damping flap $B_{77}^{(11)}$

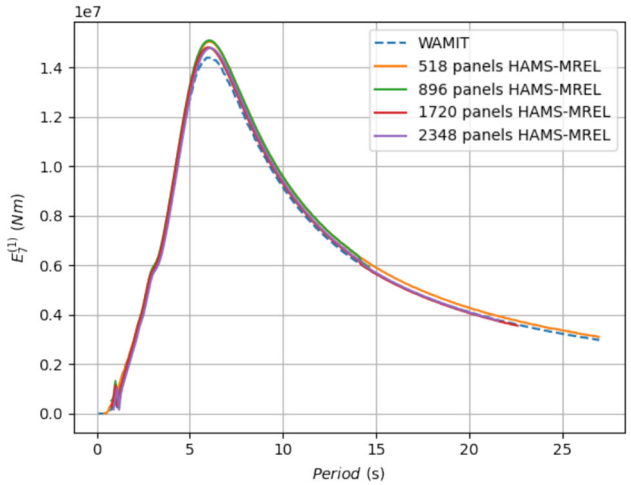

Fig. 17 Excitation force flap $E_7^{(1)}$

A mesh convergence study for the flap top was conducted to examine potential improvements in the added mass estimates from HAMS-MREL, with the outcomes also depicted in Fig. 15, 16, and 17. The results demonstrate that increasing mesh resolution significantly enhances the agreement between HAMS-MREL and WAMIT, notably for the added mass coefficient $A_{77}^{(11)}$. With 1720 panels, the results from both solvers align closely up to 14 s, with HAMS-MREL showing only a slight underestimation (less than 3%) beyond this range. It should again be emphasized that WAMIT's mesh resolution used here is lower than the converged resolution, thus minor discrepancies when using higher-resolution meshes are expected.

Additionally, computational performance for the 1720-panel mesh was measured both with and without parallelization, considering 270 frequencies and 7 degrees of freedom for the flap top. The results, presented in Table 7, indicate a computational efficiency gain factor of 16.9 when employing parallelization across 32 cores.

Table 7 Computation time for the simulations (generalized modes)

Simulation	N_P^T	N_ω	Time/frequency (sec)	Computation gain (–)
No parallelization (1 core)	1720	270	49.6	1.0
Parallelization (32 cores)	1720	270	2.93	16.9

4 Conclusions

This paper presents the theoretical background and validation of several significant enhancements implemented in the Boundary Integral Equation Method (BIEM) solver, HAMS-MREL. These new features include computation of free-surface elevation and pressure fields (collectively referred to as wave fields), global symmetry capabilities, suppression of irregular frequencies, and a generalized modes (dry modes) approach.

Regarding wave fields, validation is performed using a three-cylinder array arranged in a triangular configuration. Cross-model validation with the commercial solver WAMIT demonstrates excellent agreement in both the Response Amplitude Operators (RAOs) and the wave fields. The RAOs from both solvers match very closely, while the diffraction and radiation free surface elevation fields agree remarkably well, exhibiting differences of less than 2%.

The implementation of global symmetry is validated using a single-line arrangement of three cylinders. Hydrodynamic coefficients and excitation forces remain consistent with and without the application of symmetry, confirming the accuracy and efficiency of this feature.

The suppression of irregular frequencies feature is validated using the same three-cylinder configuration. HAMS-MREL successfully suppresses these irregular frequencies by employing a water plane mesh to solve the extended BIEM problem.

Validation of the generalized modes approach is demonstrated using a two-body flap configuration, where the flap bottom remains stationary. The shape function employed originates from our previous research (Raghavan et al. 2024d) and is validated against WAMIT results. Initial discrepancies observed in the pitch added mass coefficient using 518 panels are significantly reduced (less than 3%) when the mesh resolution is increased to 1720 panels. This highlights the importance of mesh convergence studies for accurate hydrodynamic modeling.

OpenMP parallelization has been implemented for the aforementioned features. This allows for speed-up ratios of 13.5 to 47.2 depending on the feature, from 1 core to 32 cores.

Through these enhancements, the solver HAMS-MREL is substantially improved, providing an essential computational tool to support the offshore renewable energy industry. The authors aim to significantly contribute to the advancement of the open-source community, enabling the development and deployment of highly accurate and computationally efficient numerical modeling tools critical for optimizing marine renewable energy arrays.

Acknowledgements The authors would like to thank Yingyi Liu, the creator of HAMS for the initial discussions regarding the original code. Without his original robust code, this implementation would not have been possible. The authors would like to thank Jos Van'T Hoff for sharing his results, as part of his PhD dissertation for the flap, as well as the wave fields, which have been utilized for validation. The authors would also like to thank and acknowledge the discussions with Georgia Sismani, Eva Loukogeogaki, Nikos Mantadakis and Matthieu Ancellin. The authors would also like to acknowledge SURF and access to the HPC Snellius for running the simulations in HAMS-MREL, under project EINF3290.

Author Contributions Vaibhav Raghavan: Writing – original draft, Validation, Software, Methodology, Investigation, Formal analysis, Data curation, Conceptualization. Andrei V Metrikine: Writing – review & editing, Supervision, Resources, Methodology, Conceptualization George Lavidas: Writing – review & editing, Supervision, Resources, Methodology, Investigation, Conceptualization.

No datasets were generated or analysed during the current study.

Code availability HAMS-MREL v1.0 is currently available as a binary both for Windows (https://doi.org/10.4121/1ba9ae9a-c1d5-4886-ada8-33072e4dff7d.v2) that can be used directly. The features introduced in this paper are part of the HAMS-MREL v2.0, which will be made open-source along with the source code. The code will be available on Gitlab as well as the MREL website (under the tab Datasets & Models) - www.tudelft.nl/ceg/mrel. The Marine Renewable Energies Lab (MREL) promotes and favors use of the HAMS-MREL solver for commercial and non-commercial purposes under the Apache−2.0 to include proper attribution. For all enquiries on the HAMS-MREL solver, please contact George Lavidas: `g.lavidas@tudelft.nl`, and Vaibhav Raghavan: `v.raghavan@tudelft.nl`.

Declarations

Conflict of interest The authors declare no Conflict of interest.

References

Alves M (2016) Chapter 2—frequency-domain models. In: Folley M (ed) Numerical modelling of wave energy converters. Academic Press, pp. 11-30. https://www.sciencedirect.com/science/article/pii/B9780128032107000025

Ancellin M, Dias F (2019) Capytaine: a python-based linear potential flow solver. J Open Sour Softw 4:1341. https://doi.org/10.21105/joss.01341

Ancellin M, Nguyen N (2024) Case studies of BEM solver accuracy with the open-source code capytaine. In: International Conference on Offshore Mechanics and Arctic Engineering (Vol. 87851, p. V007T09A076). American Society of Mechanical Engineers

ANSYS (2012) Ansys aqwa v14.5. In: Computer software manual

Babarit A, Delhommeau G (2015) Theoretical and numerical aspects of the open source BEM solver NEMOH. In: 11th European Wave and Tidal Energy Conference (EWTEC2015). Nantes, France. https://hal.science/hal-01198800

Balitsky P, Verao Fernandez G, Stratigaki V, Troch P (2017) Coupling methodology for modelling the near-field and far-field effects of a wave energy converter. In: International Conference on Offshore Mechanics and Arctic Engineering (Vol. 57786, p. V010T09A029). American Society of Mechanical Engineers

Chau F (1989) The second order velocity potential for diffraction of waves by fixed offshore structures. Doctoral dissertation, University College London, London

Chau FP, Taylor RE (1992) Second-order wave diffraction by a vertical cylinder. J Fluid Mech 240:571–599. https://doi.org/10.1017/S0022112092000211

De Chowdhury S, De La Cruz R, Huynh TV, Winship B, Manasseh R (2016) Computation of power from an array of wave energy converters using a boundary element method. In: 20th Australasian fluid mechanics conference, Perth, Australia. https://doi.org/10.25916/sut.26229065.v1

DNV (2023) SESAM user manual. Wadam V10.3-02

Guo Y, Yu Y-H, van Rij J, Tom N (2018) Inclusion of structural flexibility in design load analysis for wave energy converters. National Renewable Energy Lab.(NREL), Golden, CO (United States)

Herdayanditya I, Baert B, Stempinski F, Rauwoens P, Lataire E (2024) Application of irregular frequency removal feature in capytaine for anode cage installation over a monopile wind turbine, vol. 5A. Ocean Engineering. https://doi.org/10.1115/OMAE2024-126801

Kashiwagi M, Endo K, Yamaguchi H (2005) Wave drift forces and moments on two ships arranged side by side in waves wave drift forces and moments on two ships arranged side by side in waves. Ocean Eng 32(5):529–555. https://doi.org/10.1016/j.oceaneng.2004.09.005 (https://www.sciencedirect.com/science/article/pii/S0029801804002252)

Kelly T, Zabala I, Peña-Sanchez Y, Penalba M, Ringwood JV, Henriques JC, Blanco JM (2022) A post-processing technique for removing 'irregular frequencies' and other issues in the results from bem solvers. Int Marine Energy J 5(1):123–131. https://doi.org/10.36688/imej.5.123-131 (https://marineenergyjournal.org/imej/article/view/114)

Kurnia R, Ducrozet G (2023) Nemoh: open-source boundary element solver for computation of first- and second-order hydrodynamic loads in the frequency domain. Comput Phys Commun 292:108885. https://doi.org/10.1016/j.cpc.2023.108885 (https://www.sciencedirect.com/science/article/pii/S0010465523002308)

Lee C-H, Newman JN (2003) Computation of wave effects using the panel method. Retrieved from https://api.semanticscholar.org/CorpusID:17331425

Lee CH, Newman JN (2006) Wamit user manual, versions 7, 6.4, 6.4pc, 6.3s, 6.3s-pc. In: Computer software manual

Li G, Stansby P (2023) Software framework to accelerate BEM linear wave load program using OpenMP (OREGEN-BEM). In: The 33rd international ocean and polar engineering conference, Ottawa, Canada

Li G, Stansby P (2024) Hydrodynamic analysis of different configurations of the m4 wave energy converter system using oregen. Ocean Renew Energy. https://doi.org/10.1115/OMAE2024-123824

Li G, Stansby P, Draycott S (2024) General formulation for floating body with elastic mooring in irregular waves: a hybrid linear and nonlinear framework and validation. Mar Struct 96:103623. https://doi.org/10.1016/j.marstruc.2024.103623 (https://www.sciencedirect.com/science/article/pii/S0951833924000510)

Liu Y (2019) HAMS: a frequency-domain preprocessor for wave-structure interactions–theory, development, and application. J Marine Sci Eng. https://doi.org/10.3390/jmse7030081. https://www.mdpi.com/2077-1312/7/3/81

Liu Y, Yoshida S, Hu C, Sueyoshi M, Sun L, Gao J, He G (2018) A reliable open-source package for performance evaluation of floating renewable energy systems in coastal and offshore regions. Energy Convers Manage 174:516–536. https://doi.org/10.1016/j.enconman.2018.08.012 (https://www.sciencedirect.com/science/article/pii/S0196890418308562)

Mankle H, Yu Y-H, DuPont B (2019) Wec-sim array development and experimental comparison study. Natil Renew Energy Lab. https://www.nrel.gov/docs/fy20osti/74083.pdf

Marburg S, Amini S (2005) Cat's eye radiation with boundary elements: comparative study on treatment of irregular frequencies. J Comput Acoust. https://doi.org/10.1142/S0218396X05002566

Matsui T, Kato K, Shirai T (1987) A hybrid integral equation method for diffraction and radiation of water waves by three-dimensional bodies. Comput Mech 2:119–135. https://doi.org/10.1007/BF00282134 (https://doi-org.tudelft.idm.oclc.org/10.1007/BF00282134)

Newman J (1994) Wave effects on deformable bodies. Appl Ocean Res 16(1):47–59. https://doi.org/10.1016/0141-1187(94)90013-2 (https://www.sciencedirect.com/science/article/pii/0141118794900132)

ORCINA (2023) Orcawave v11.4e. In: Computer software manual

Quartier N, Vervaet T, Fernandez GV, Domínguez JM, Crespo AJ, Stratigaki V, Troch P (2024) High-fidelity numerical modelling of a two-wec array with accurate implementation of the pto system and control strategy using dualsphysics. Energy 296:130888. https://doi.org/10.1016/j.energy.2024.130888 (https://www.sciencedirect.com/science/article/pii/S0360544224006601)

Raghavan V, Loukogeorgaki E, Mantadakis N, Metrikine AV, Lavidas G (2024) Hams-mrel, a new open source multiple body solver for marine renewable energies: model description, application and validation. Renew Energy 237:121577. https://doi.org/10.1016/j.renene.2024.121577 (https://www.sciencedirect.com/science/article/pii/S0960148124016458)

Raghavan V, Simonetti I, Metrikine AV, Lavidas G, Cappietti L (2024) A new numerical modelling framework for fixed oscillating water column wave energy conversion device combining bem and cfd methods: validation with experiments. Ocean Eng 301:117543. https://doi.org/10.1016/j.oceaneng.2024.117543 (https://www.sciencedirect.com/science/article/pii/S0029801824008801)

Raghavan V, Lavidas G, Metrikine AV (2024) Comparing open-source bem solvers for analysing wave energy converters. J Phys: Conf Ser. https://doi.org/10.1088/1742-6596/2647/7/072002. https://dx.doi.org/10.1088/1742-6596/2647/7/072002

Raghavan V, Metrikine A, Lavidas G, Islam T, Venugopal V (2024) Extension of hams with the generalized modes approach. In: Soares C, Wang S (eds) Innovations in renewable energies offshore—proceedings of the 6th international conference on renewable energies offshore, renew 2024 (pp. 193–199). CRC Press/Balkema - Taylor and Francis Group. 6th International Conference on Renewable Energies Offshore, RENEW 2024; Conference date: 19-11-2024 Through 21-11-2024

Sheng W, Tapoglou E, Ma X, Taylor C, Dorrell R, Parsons D, Aggidis G (2022) Hydrodynamic studies of floating structures: comparison of wave-structure interaction modelling. Ocean Eng 249:110878. https://doi.org/10.1016/j.oceaneng.2022.110878 (https://www.sciencedirect.com/science/article/pii/S0029801822003183)

Sismani G, Loukogeorgaki E (2020) Frequency-based investigation of a floating wave energy converter system with multiple flaps. Appl Math Model 84:522–535. https://doi.org/10.1016/j.apm.2020.04.013 (https://www.sciencedirect.com/science/article/pii/S0307904X20302067)

Sun L, Stansby P, Zang J, Moreno E, Taylor P (2016) Linear diffraction analysis for optimisation of the three-float multi-mode wave energy converter m4 in regular waves including small arrays. J Ocean Eng Marine Energy 2:429–438. https://doi.org/10.1007/s40722-016-0059-1

van Rij J, Yu Y-H, Guo Y (2017) Structural loads analysis for wave energy converters, vol. 10. In: Ocean Renewable Energy. https://doi.org/10.1115/OMAE2017-62139

Van'T Hoff J (2009) Hydrodynamic modelling of the oscillating wave surge converter. Doctoral dissertation. Queens University Belfast

Verao Fernandez G, Balitsky P, Stratigaki V, Troch P (2018) Coupling methodology for studying the far field effects of wave energy converter arrays over a varying bathymetry. Energies. https://doi.org/10.3390/en11112899. https://www.mdpi.com/1996-1073/11/11/2899

Verao Fernandez G, Balitsky P, Stratigaki V, Troch P (2018) Validation of a coupling methodology for numerical modelling of near and far field effects of Wave Energy Converter arrays using the MILD-wave and NEMOH models, based on the WECwakes experimental database. In: Book of Abstracts Special Publication, vol. 80, pp. 124–125

Verbrugghe T, Stratigaki V, Troch P, Rabussier R, Kortenhaus A (2017) A comparison study of a generic coupling methodology for modeling wake effects of wave energy converter arrays. Energies. https://doi.org/10.3390/en10111697

Veritas B (2024) Hydrostar hydrodynamic solver. https://marine-offshore.bureauveritas.com/hydrostar-software-powerful-hydrodynamic [Online; accessed 12-December-2024]

Vervaet T, Quartier N, Carpintero Moreno E, Verao Fernandez G, Ferri F, Stratigaki V, Troch P (2024) System identification and centralised causal impedance matching control of a row of two heaving point absorber wave energy converters. Ocean Eng 309:118399. https://doi.org/10.1016/j.oceaneng.2024.118399 (https://www.sciencedirect.com/science/article/pii/S0029801824017372)

Wolgamot H, Taylor PE, Taylor R (2012) The interaction factor and directionality in wave energy arrays. Ocean Eng 47:65–73. https://doi.org/10.1016/j.oceaneng.2012.03.017 (https://www.sciencedirect.com/science/article/pii/S0029801812001138)

Wolgamot H, Eatock Taylor R, Taylor P (2016) Effects of second-order hydrodynamics on the efficiency of a wave energy array. Int J Marine Energy 15: 85-99. (Selected Papers from the European Wave and Tidal Energy Conference 2015, Nante, France). https://doi.org/10.1016/j.ijome.2016.04.005. https://www.sciencedirect.com/science/article/pii/S2214166916300170